



Thermo-poroelastic modelling of cement sheath: pore pressure response, thermal effect and thermo-osmotic effect

Zihua Niu, Jiyun Shen, Linlin Wang & Rongwei Yang

To cite this article: Zihua Niu, Jiyun Shen, Linlin Wang & Rongwei Yang (2019): Thermo-poroelastic modelling of cement sheath: pore pressure response, thermal effect and thermo-osmotic effect, European Journal of Environmental and Civil Engineering, DOI: [10.1080/19648189.2019.1675094](https://doi.org/10.1080/19648189.2019.1675094)

To link to this article: <https://doi.org/10.1080/19648189.2019.1675094>



Published online: 21 Oct 2019.



Submit your article to this journal [↗](#)



Article views: 11



View related articles [↗](#)



View Crossmark data [↗](#)



Thermo-poroelastic modelling of cement sheath: pore pressure response, thermal effect and thermo-osmotic effect

Zihua Niu^{a,b}, Jiyun Shen^c, Linlin Wang^d and Rongwei Yang^{a,b}

^aSchool of Civil Engineering, Tianjin University, Tianjin, P.R. China; ^bKey Laboratory of Coast Civil Structure Safety of Ministry of Education, Tianjin University, Tianjin, P.R. China; ^cCNPC Engineering Technology R&D Company Limited, Beijing, P.R. China; ^dCollege of Petroleum Engineering, China University of Petroleum (Beijing), Beijing, P.R. China

ABSTRACT

Cement sheath provides zonal isolation and structural support during oil/gas well exploitation. Mechanical behaviours of cement sheath are of increasing concern with the exploitation of shale gas. In order to overcome the drawbacks of continuum assumption of cement sheath, a comprehensive thermo-poroelastic model, accounting for the pore water pressure resulted from hydraulic pressure in casing, the thermal loading induced by the temperature difference between the injected water in casing and underground formation, and thermo-osmotic effect, is developed to determine the evolution of effective stress of cement sheath. Moreover, failure criteria for the cement sheath, whose parameters are temperature dependent, are proposed to assess failure modes of cement sheath. A case study is also carried out to assess the tendencies of the failure modes of cement sheath during loading. Application of the proposed model on a triaxial test of undrained heating of oil well cement paste shows the capability of the model with $k_{pT} = 5 \times 10^{-12} \text{m}^2/(\text{°C}\cdot\text{s})$ to well reproduce the experimental results.

ARTICLE HISTORY

Received 13 May 2019
Accepted 25 September 2019

KEYWORDS

Cement sheath; thermo-poroelastic model; thermo-osmotic effect; effective stress; failure criteria

1. Introduction

With the rapid development and improvement of hydraulic fracturing, shale gas is becoming crucial unconventional energy source over the past decades (De Andrade & Sangesland, 2016; Gao et al., 2017). A typical illustration of shale gas well consists of: (1) steel casing(s); (2) cement sheath and (3) the surrounding formation (see Figure 1). For a casing-cement sheath-formation (CCF) system, cement sheath provides structural support and zonal isolation during the production of shale gas (Petersen, 2015). The integrity and sealing properties of cement sheath during the exploitation of shale gas are more and more concerned by petroleum engineers. Among all the causes of failure of cement sheath, radial cracks within cement sheath and debonding between casing-cement sheath interface during the production process are two of the most significant ones (De Andrade & Sangesland, 2016).

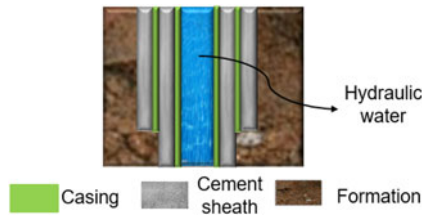


Figure 1. Schematic illustration of casing-cement sheath-formation (CCF) system.

In order to assess the sealing properties and integrity of cement sheath, the stress distribution of cement sheath should be known first. Generally, the stress distribution of cement sheath is largely influenced by the following two factors: (1) pore water pressure evolution of the cement sheath (Petersen, 2015); (2) thermal loading caused by the temperature difference between the injected water and the underground formation.

Over the past decades, extensive hydro-thermal-mechanical models for oil wellbore have been developed (Gao et al., 2017; Gelet, Loret, & Khalili, 2012; Kanfar, Chen, & Rahman, 2017; Loh et al., 2014; Wang et al., 2014, 2015; Wang & Dusseault, 2003). According to the preceding studies, it has been found that the thermal loading within underground formation plays a crucial role in the stability of the wellbore and should not be neglected (Falser, Uchida, Palmer, Soga, & Tan, 2012). When it comes to CCF system, numerous methods, either analytical ones or numerical ones have been employed to analyse the stress field in cement sheath throughout the entire life cycle of the well (Ardakani & Ulm, 2013; Ghassemi, Tao, & Diek, 2009; Shi, Li, Guo, Guan, & Li, 2015; Xia, Jin, Chen, & Lu, 2017; Zhang & Wang, 2017). However, the cement sheath was still considered to be elastic continuum medium and thus the effect of pore pressure on the mechanical behaviour of cement sheath was neglected in the previous works.

In nature, cement sheath is a kind of porous material, consisting of several types of pore space, i.e. interlayer space, gel pores, capillary pores and air voids, ranging from several nanometres to several hundred microns. However, as introduced previously, the evolution of pore pressure in the cement sheath, which is expected to play a vital role in hydro-mechanical behaviours of cement sheath, was not fully accounted for in the existing studies. Moreover, a ubiquitous thermo-osmosis (Derjaguin & Sidorenkov, 1941; Ghassemi et al., 2009), characterizing liquid flow through capillaries or porous materials applied on a temperature gradient, becomes essential in a porous material with finer pore size. Based on numerical simulation, thermo-osmotic (T-O) effect was accounted for to analyse the effect of high salinity mud on wellbore stability by Ghassemi et al. (2009), and it was found that such effect increased the potential tensile failure of wellbore. Several experiments were carried out to measure the T-O coefficient of various types of formation (Kim & Mench, 2009; Trémosa, Gonçalves, Matray, & Violette, 2010; Zheng & Samper, 2008). However, to the best of our knowledge, few work has been carried out to study the T-O effect on thermo-poromechanical behaviour of cement sheath so far.

Based on the work of Cheng (2016), the purpose of this research is to develop a thermo-poroelastic model for assessing the integrity of cement sheath in CCF system. Pore water pressure of cement sheath induced by hydraulic pressure in casing, thermal loading induced by the temperature difference between injected water and formation, and T-O effect in cement sheath are fully accounted for in the proposed model. The article is organised as follows: in Section 2, a thermo-poroelastic model for the CCF system as well as a failure criterion for cement sheath are developed. The poroelastic effects, thermal loading and T-O effects on the distribution and evolution of the effective stress of cement sheath are discussed in Section 3, respectively; parametric analyses are also carried out in this section. In Section 4, the proposed model is used to simulate

a test on undrained heating of oil well cement paste, moreover, a case study is carried out in this section. Main conclusions are summarised in [Section 5](#).

2. Model development

2.1. Assumptions

The proposed thermo-poro-elastic model is based on the following assumptions (Cheng, 2016):

1. The casing, cement sheath and formation are all linear plain strain.
2. Both cement sheath and formation are regarded as fully saturated.
3. The pore water is assumed to be compressible.
4. Through pore water diffusion and heat conduction, temperatures of pore water and solid phase in the same representative volume element (RVE) always remain the same.
5. The permeabilities of formation and cement sheath are low. Their intrinsic permeabilities are typically less than 10^{-15} m, which leads to a further assumption that heat flux is transported solely by conduction instead of convection.

2.2. Governing equations

1. Constitutive equations

$$\begin{cases} \sigma_{ij} = 2G^{cas} \left[\varepsilon_{ij} - \frac{1}{3} \delta_{ij} \beta^{cas} \Delta T + \frac{\nu^{cas}}{1 - 2\nu^{cas}} \delta_{ij} (\varepsilon - \beta^{cas} \Delta T) \right] & \text{For casing} \\ \sigma_{ij} = 2G^y \left[\varepsilon_{ij} + \frac{\nu^y}{1 - 2\nu^y} \delta_{ij} \varepsilon \right] - \alpha^y \delta_{ij} p - \omega_d^y \delta_{ij} \Delta T & \text{For cement sheath/formation} \end{cases} \quad (1)$$

in which σ_{ij} and ε_{ij} represent the total stress and the total strain tensor, respectively; ε denotes the volumetric strain; ΔT denotes the variation of temperature between injected water and formation; β^y denotes volumetric thermal expansion coefficient of the material; δ_{ij} is the Kronecker delta; G^y , ν^y denote shear modulus and Poisson's ratio, respectively; α^y denotes Biot's coefficient; $\omega_d^y = K^y \beta^y$ represents drained thermoelastic effective stress coefficient; p is the variation of pore water pressure relative to the reference state; the superscript y can be cem for cement sheath or for for formation; the superscript cas denotes casing.

Another two state equations, one characterizing the variation of pore water volume in a RVE of porous material ζ , the other characterizing the total entropy density in porous material s_h , are given as follows

$$\zeta = \alpha^y \varepsilon + \frac{p}{N^y} - \beta_e^y \Delta T \quad (2)$$

$$s_h = \omega_d^y \varepsilon - \beta_e^y p + m_d^y \Delta T \quad (3)$$

where $1/N^y = (\alpha^y - \phi_0^y)/K_s^y$ (Dormieux, Kondo, & Ulm, 2006); ϕ_0^y denotes porosity; K_s^y is bulk modulus of solid phase; $\beta_e^y = \alpha \beta_s^y + \phi_0^y (\beta_f - \beta_s^y)$ is volumetric thermal expansion coefficient for variation in pore water content at constant frame volume (Cheng, 2016); β_s^y and β_f denote volumetric thermal expansion coefficients of solid phase of porous materials and pore water, respectively; $m_d^y = \frac{c_d^y}{T_0^y}$, in which c_d^y and T_0^y are the drained specific heat at constant strain and the initial temperature, respectively.

2. Strain–displacement relations

$$\varepsilon_{ij} = \frac{1}{2}(u_{i,j} + u_{j,i}) \quad (4)$$

where u_i denotes the displacement vector.

3. Equilibrium equations

Momentum equilibrium:

$$\sigma_{ij,j} = 0 \quad (5)$$

Fluid mass equilibrium:

$$\frac{\partial(\rho^f \zeta)}{\partial t} + \nabla \cdot (\rho^f \vec{q}_f) = 0 \quad (6)$$

where \vec{q}_f denotes the pore water flux vector and ρ^f denotes density of pore water. The expansion of Equation (6) writes

$$\zeta \frac{\partial \rho^f}{\partial t} + \vec{q}_f \cdot \nabla \rho^f + \rho^f \left(\frac{\partial \zeta}{\partial t} + \nabla \cdot \vec{q}_f \right) = 0 \quad (7)$$

The first and the second terms in Equation (7) can be proved to be two degrees of magnitude smaller than the remaining terms. Therefore, Equation (7) can be simplified as

$$\frac{\partial \zeta}{\partial t} + \nabla \cdot \vec{q}_f \approx 0 \quad (8)$$

Thermal energy equilibrium:

$$\Delta T \frac{\partial s_h}{\partial t} + \nabla \cdot \vec{q}_h = 0 \quad (9)$$

where \vec{q}_h denotes homogeneous thermal flux in porous material.

Different from Darcy's law for fluid transport and Fourier's law for thermal conduction, when porous material is subjected to the coupling of fluid and thermal fields, both T-O effect and mechano-caloric effect should be accounted for based on Onsager's reciprocity (Derjaguin & Sidorenkov, 1941; Kurashige, 1992). Therefore, the constitutive equations for thermal flux and fluid flux in porous materials read

$$\vec{q}_f = -\kappa^y \nabla p - k_{pT}^y \nabla(\Delta T) \quad (10)$$

$$\vec{q}_h = -k_{Tp}^y \nabla p - k_T^y \nabla(\Delta T) \quad (11)$$

where the superscript y can be cem for cement sheath or for formation; κ^y denotes permeability of porous material, k_T^y is effective thermal conductivity of porous material; k_{Tp}^y denotes the mechano-caloric coefficient which characterises the effect of pore water pressure gradient on the thermal conduction (Gonçalvès & Trémosa, 2010) while k_{pT}^y is the T-O coefficient which characterises the effect of temperature gradient on the fluid diffusivity (Derjaguin & Sidorenkov, 1941; Yang, Gui, Lemarchand, Fen-Chong, & Li, 2015; Yang, Lemarchand, & Fen-Chong, 2016; Yang, Li, Lemarchand, & Fen-Chong, 2016).

As pointed out by Carnahan (1983), thermo-osmosis induced fluid flux (i.e. $k_{pT}^y \nabla(\Delta T)$ in Equation (10)) can be eight hundred times greater than that resulting from pressure gradient (i.e. $\kappa^y \nabla p$ in Equation (10)). Whereas, as argued by Ghassemi et al. (2009), compared with thermal conduction (i.e. $k_T^y \nabla(\Delta T)$ in Equation (11)), mechano-caloric effect (i.e. $k_{Tp}^y \nabla p$ in Equation (11))

can be neglected. Therefore, Equations (10) and (11) can be reformulated as

$$\vec{q}_f = -\kappa^y \nabla p - k_{pT}^y \nabla (\Delta T) \quad (12)$$

$$\vec{q}_h = -k_T^y \nabla (\Delta T) \quad (13)$$

As regards T-O coefficient of cement, scarce experimental data have been found in literatures. As an alternative, several T-O coefficients of formations have been determined: $3.62 \times 10^{-12} \text{m}^2/(\text{°Cs})$ for a bentonite engineered barrier (Zheng & Samper, 2008), $6 \times 10^{-12} \text{m}^2/(\text{°Cs})$ to $2 \times 10^{-10} \text{m}^2/(\text{°Cs})$ for Liassic argillite formation (Gonçalvès & Trémosa, 2010; Trémosa et al., 2010). Moreover, T-O coefficient of a material k_{pT} is closely related to its intrinsic permeability k by $k_{pT} = k\varepsilon_T/\mu$, where μ is the dynamic viscosity of pore water, $\varepsilon_T = \Delta H/T$, ΔH is the macroscopic constant mean value of the excess enthalpy, which is related to temperature T , mean half pore size as well as the disjoining pressure of the material (Gonçalvès, Ji Yu, Matray, & Trémosa, 2018; Gonçalvès & Trémosa, 2010; Trémosa et al., 2010). As pointed out by Gonçalvès and Trémosa (2010), when the mean half pore size of formations is small, corresponding to the case of finer pores when the water cement ratio of cement sheath is low, the T-O coefficient of cement sheath can be as high as $1 \times 10^{-10} \text{m}^2/(\text{°Cs})$. On the contrary, when the cement sheath has larger mean pore size (associated with large water to cement ratio), T-O coefficient can be smaller than $k_{pT} \leq 1 \times 10^{-12} \text{m}^2/(\text{°Cs})$.

2.3. Boundary conditions

The boundary conditions illustrated in Figure 2 are based on the following assumptions: (1) both casing and cement sheath are concentric; (2) under the applied loading conditions, there is no debonding occurring in casing-cement sheath and cement sheath-formation interfaces; (3) initial geostatic stress in the formation is isotropic and, thus, the CCF system is axial symmetric; (4) temperature variation in the formation is neglected since there may be other underground heat source, e.g. geothermal energy. As shown in Figure 2, the thermal and mechanical boundaries write:

1. at the inner interface of the casing ($r = r_1$):

$$\sigma_{rr}^{cas}(r_1) = -p_i \quad (14)$$

where p_i denotes the hydraulic pressure inside the casing.

2. at the casing-cement sheath interface ($r = r_2$):

$$\Delta T(r_2) = \Delta T_0 \quad (15)$$

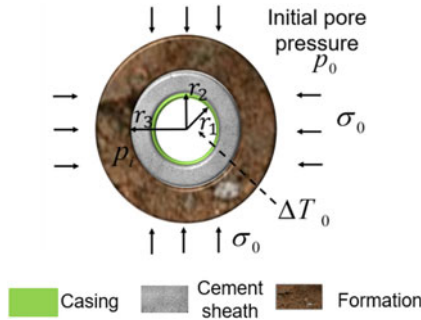


Figure 2. 2-D schematic illustration and boundary conditions of casing-cement sheath-formation (CCF) system. r_1 , r_2 and r_3 denote inner radius of casing, outer radius of casing (i.e. inner radius of cement sheath) and outer radius of cement sheath, respectively, ΔT_0 is the temperature difference between the hydraulic water and the underground formation, σ_0 is far-field geostatic stress in formation.

$$\sigma_{rr}^{cas}(r_2) = \sigma_{rr}^{cem}(r_2) \quad (16)$$

$$u_r^{cas}(r_2) = u_r^{cem}(r_2) \quad (17)$$

$$q_r^{cem}(r_2) = 0 \quad (18)$$

where u_r is radial displacement; q_r is radial fluid flux; σ_{rr} is radial stress and $\Delta T_0 = T_0^w - T_0^f$ is the temperature difference between the injected water (T_0^w) and the underground formation (T_0^f).

3. at the cement sheath-formation interface ($r = r_3$):

$$\Delta T(r_3) = 0 \quad (19)$$

$$q_r^{cem}(r_3) = q_r^{for}(r_3) \quad (20)$$

$$p^{cem}(r_3) = p^{for}(r_3) \quad (21)$$

$$u_r^{cem}(r_3) = u_r^{for}(r_3) \quad (22)$$

$$\sigma_{rr}^{cem}(r_3) = \sigma_{rr}^{for}(r_3) \quad (23)$$

where p denotes the increment of pore water pressure after loading.

4. at the infinity ($r \rightarrow \infty$):

$$\Delta T(r \rightarrow \infty) = 0 \quad (24)$$

$$\sigma_{rr}^{for}(r \rightarrow \infty) - \sigma_0 = -\sigma_0 \quad (25)$$

$$p^{for}(r \rightarrow \infty) + p_0 = p_0 \quad (26)$$

where σ_{ij}^y ($y = cas, cem$ or for ; $i = r$ or θ) denotes the variation of total stress after loading, $-\sigma_0$ (negative sign denotes compressive stress) is the initial far-field geostatic stress in formation and p_0 is the initial far-field pore pressure.

2.4. General solutions

2.4.1. Solutions for cement sheath

Combining Equations (1)–(9) and Equations (12) and (13) yields the following two equations for cement sheath

$$\begin{cases} \frac{\partial(\Delta T)^{cem}}{\partial t} - c_a^{cem} \nabla^2 (\Delta T)^{cem} = \frac{\beta_c^{cem}}{S_a^{cem}} \frac{\partial p^{cem}}{\partial t} - \frac{\eta_d^{cem}(1-\nu^{cem})}{S_a^{cem}(1-2\nu^{cem})} \frac{dg^{cem}}{dt} \\ \frac{\partial p^{cem}}{\partial t} - c^{cem} \nabla^2 p^{cem} = \frac{\beta_c^{cem}}{S^{cem}} \frac{\partial(\Delta T)^{cem}}{\partial t} - \frac{\alpha^{cem}}{S^{cem}} \frac{dg^{cem}}{dt} + \frac{k_p^{cem}}{S^{cem}} \nabla^2 (\Delta T)^{cem} \end{cases} \quad (27)$$

where $S^{cem} = 1/N^{cem} + 3(\alpha^{cem})^2/(3K^{cem} + 4G^{cem})$, $c^{cem} = \kappa^{cem}/S^{cem}$, $\kappa^{cem} = k^{cem}/\mu$, k^{cem} denotes intrinsic permeability of cement sheath; μ is the dynamic viscosity of pore water; $\eta^{cem} = \alpha^{cem}(1-2\nu^{cem})/[2(1-\nu^{cem})]$, $c_a^{cem} = k_T^{cem}/(S_a^{cem}T_0)$, $S_a^{cem} = m_d^{cem}(3K_a^{cem} + 4G^{cem})/(3K^{cem} + 4G^{cem})$, $K_a^{cem} = K^{cem} + (\omega_d^{cem})^2/m_d^{cem}$, $\beta_c^{cem} = \phi_0^{cem}(\beta_r - \beta_s^{cem}) + \frac{4}{3}\eta^{cem}\beta_s^{cem}$ and $\eta_d^{cem} = \omega_d^{cem}(1-2\nu^{cem})/[2(1-\nu^{cem})]$; g^{cem} is a constant in Laplace domain to be determined later.

In the case of oil cement, it can be proved that the magnitude of the thermal elastic coupling term $\frac{K^{cem}(\beta_s^{cem})^2 T_0^{cem}}{c_d^{cem}}$ is of the order of 10^{-3} . According to Zimmerman (2000), if $\frac{K^{cem}(\beta_s^{cem})^2 T_0^{cem}}{c_d^{cem}} \ll 1$, Equation (27) can be further simplified as

$$\begin{cases} \frac{\partial(\Delta T)^{cem}}{\partial t} - \kappa_T^{cem} \nabla^2 (\Delta T)^{cem} = 0 \\ \frac{\partial p^{cem}}{\partial t} - c^{cem} \nabla^2 p^{cem} = \frac{\beta_c^{cem} + \frac{\kappa_{pT}^{cem}}{\kappa_T^{cem}}}{s^{cem}} \frac{\partial(\Delta T)^{cem}}{\partial t} - \frac{\alpha^{cem}}{s^{cem}} \frac{dg^{cem}}{dt} \end{cases} \quad (28)$$

where $\kappa_T^{cem} = \kappa_T^{cem}/c_d$ is heat diffusivity coefficient.

Equation (28) can be solved by means of Laplace transform and numerical method for inverse Laplace transform (Abousleiman & Kanj, 2004; Detournay & Cheng, 1988; Gao et al., 2016). Solving Equation (28) in Laplace domain, we obtain the solutions for temperature and stress distribution of cement sheath as follow (the detailed derivation is given in Appendix A)

$$\Delta T^{cem^\circ} = C_1 I_0(\zeta_T^{cem}) + C_2 K_0(\zeta_T^{cem}) \quad (29)$$

$$p^{cem^\circ} = a^{cem} \Delta T^{cem^\circ} + b^{cem} \quad (30)$$

$$p^{cem^\circ} = p^{cem^\circ} + C_3 I_0(\zeta_p^{cem}) + C_4 K_0(\zeta_p^{cem}) \quad (31)$$

$$\begin{aligned} u_r^{cem^\circ} = & C_5 r + C_6 \frac{1}{r} + \frac{\eta^{cem}}{G^{cem}} \left[a^{cem} \left(C_1 \frac{I_1(\zeta_T^{cem})}{\zeta_T^{cem}} r - C_2 \frac{K_1(\zeta_T^{cem})}{\zeta_T^{cem}} r \right) + \frac{b^{cem}}{2} r \right] \\ & + \frac{\eta^{cem}}{G^{cem}} \left[C_3 \frac{I_1(\zeta_p^{cem})}{\zeta_p^{cem}} r - C_4 \frac{K_1(\zeta_p^{cem})}{\zeta_p^{cem}} r \right] \end{aligned} \quad (32)$$

$$\begin{aligned} & + \left[C_1 \frac{I_1(\zeta_T^{cem})}{\zeta_T^{cem}} r - C_2 \frac{K_1(\zeta_T^{cem})}{\zeta_T^{cem}} r \right] \frac{\eta_d^{cem}}{G^{cem}} \\ g^{cem^\circ} = & 2C_5 \end{aligned} \quad (33)$$

$$\begin{aligned} v_{rr}^{cem^\circ} = & C_5 + C_6 \frac{1}{r^2} \\ & + \frac{\eta^{cem}}{G^{cem}} \left[a^{cem} \left(C_1 \left(I_0(\zeta_T^{cem}) - \frac{I_1(\zeta_T^{cem})}{\zeta_T^{cem}} \right) + C_2 \left(K_0(\zeta_T^{cem}) + \frac{K_1(\zeta_T^{cem})}{\zeta_T^{cem}} \right) \right) \right. \\ & + \frac{b^{cem}}{2} + C_3 \left(I_0(\zeta_p^{cem}) - \frac{I_1(\zeta_p^{cem})}{\zeta_p^{cem}} \right) + C_4 \left(K_0(\zeta_p^{cem}) + \frac{K_1(\zeta_p^{cem})}{\zeta_p^{cem}} \right) \Big] \\ & + \frac{\eta_d^{cem}}{G^{cem}} \left(C_1 \left(I_0(\zeta_T^{cem}) - \frac{I_1(\zeta_T^{cem})}{\zeta_T^{cem}} \right) + C_2 \left(K_0(\zeta_T^{cem}) + \frac{K_1(\zeta_T^{cem})}{\zeta_T^{cem}} \right) \right) \end{aligned} \quad (34)$$

$$\begin{aligned} v_{\theta\theta}^{cem^\circ} = & C_5 + C_6 \frac{1}{r^2} + \frac{\eta^{cem}}{G^{cem}} \left[a^{cem} \left(C_1 \frac{I_1(\zeta_T^{cem})}{\zeta_T^{cem}} - C_2 \frac{K_1(\zeta_T^{cem})}{\zeta_T^{cem}} \right) + \frac{b^{cem}}{2} \right] \\ & + \frac{\eta^{cem}}{G^{cem}} \left[C_3 \frac{I_1(\zeta_p^{cem})}{\zeta_p^{cem}} - C_4 \frac{K_1(\zeta_p^{cem})}{\zeta_p^{cem}} \right] \\ & + \frac{\eta_d^{cem}}{G^{cem}} \left(C_1 \frac{I_1(\zeta_T^{cem})}{\zeta_T^{cem}} - C_2 \frac{K_1(\zeta_T^{cem})}{\zeta_T^{cem}} \right) \end{aligned} \quad (35)$$

$$\begin{aligned} q_r^{cem^\circ} = & -\kappa^{cem} \left(a^{cem} \sqrt{\frac{s}{\kappa_T^{cem}}} (C_1 I_1(\zeta_T^{cem}) - C_2 K_2(\zeta_T^{cem})) \right) \\ & - \kappa^{cem} \left(\sqrt{\frac{s}{c^{cem}}} (C_3 I_1(\zeta_p^{cem}) - C_4 K_1(\zeta_p^{cem})) \right) \end{aligned} \quad (36)$$

where p^{cem° denotes the specific solution of p^{cem} , $\zeta_T^{cem} = \sqrt{\frac{s}{\kappa_T^{cem}}} r$, s denotes the variable in Laplace domain transformed from the time t , $a^{cem} = \beta_c^{cem} + \kappa_{pT}^{cem}/\kappa_T^{cem} / [s(1 - \frac{c^{cem}}{\kappa_T^{cem}})]$, $b^{cem} =$

$-c_g^{cem} g^{cem^o}, \zeta_p^{cem} = \sqrt{\frac{s}{c^{cem}}} r$. Superscript o appeared in Equations (29)–(36) denotes the solution in Laplace domain. Parameters C_1 – C_6 in Equations (29)–(36) are six unknown constants to be determined by the boundary conditions, which will be presented in the following section.

2.4.2. Solutions for formation

Analogously, solutions for formation can be expressed as Equations (29)–(36) by substituting C_1 – C_6 in Equations (29)–(36) with D_1 – D_6 . However, according to Equations (19), (24) and (29), $D_1 = D_2 = 0$ can be determined. Therefore, only four parameters D_3 – D_6 are not determined.

2.4.3. Solutions for casing

For casing, combining Equations (1)–(5) yields the Navier-type equation

$$\frac{\partial e^{cas}}{\partial r} - \frac{1 + \nu^{cas}}{3(1 - \nu^{cas})} \beta^{cas} \frac{\partial \Delta T^{cas}}{\partial r} = 0 \quad (37)$$

It is assumed that temperature is uniformly distributed in the casing. Therefore, we have

$$\Delta T^{cas} = \Delta T_0 \quad (38)$$

Taking advantage of Equation (38), the second term in the left hand of Equation (37) can be omitted since ΔT_0 is constant. The solution for Equation (37) can thus be directly determined without Laplace transform. However, to be consistent with the solutions in Section 2.4.1, the general solutions for Equation (37) are expressed in Laplace domain as

$$e^{cas^o} = F_1 \quad (39)$$

$$u_r^{cas^o} = \frac{r}{2} F_1 + \frac{F_2}{r} \quad (40)$$

$$e_{rr}^{cas^o} = \frac{F_1}{2} - \frac{F_2}{r^2} \quad (41)$$

$$\sigma_{rr}^{cas^o} = 2G^{cas} \left[e_{rr}^{cas} - \frac{1}{3} \beta^{cas} \Delta T^{cas} + \frac{\nu^{cas}}{1 - 2\nu^{cas}} (e^{cas} - \beta^{cas} \Delta T^{cas}) \right] \quad (42)$$

where F_1 and F_2 are to be determined in the following section.

2.5. Determination of parameters and the solutions in time domain

Combining the general solutions in Section 2.4 and the boundary conditions in Section 2.3, the parameters C_1 – C_6 , D_3 – D_6 , F_1 and F_2 can be analytically determined.

The results presented in the previous sections are expressed in Laplace domain. In order to acquire the real solutions in time domain, a numerical inverse Laplace transform such as Stehfest algorithm (Stehfest, 1970) is employed

$$f(t) \approx \frac{\ln 2}{t} \sum_{n=1}^M C_n F\left(n \frac{\ln 2}{t}\right) \quad (43)$$

where $C_n = (-1)^{n+M/2} \sum_{k=(n+1)/2}^{\min\{n, M/2\}} \frac{k^{M/2} (2k)!}{(M/2-k)! k! (k-1)! (n-k)! (2k-n)!}$, f and F denote respectively the function in time domain and its corresponding function in Laplace domain. The value of M is even and is typically in the range of 10–20 (Detournay & Cheng, 1988).

2.6. Initial stress

In order to more faithfully evaluate the integrity of cement sheath, the initial stress brought about by the setting process of cement slurry should be accounted for in the effective stress of cement sheath (Lavrov & Torsæter, 2016). The initial stress arose from setting of cement slurry consists of two parts: (1) the hydraulic stress induced by the autogenetic weight of cement slurry during pumping, i.e. $\sigma_{ij}^{(1)} = -\rho^{cem}gh\delta_{ij}$, where ρ^{cem} denotes density of cement slurry, g is gravitational acceleration and h is the given depth of cement sheath; (2) a stress induced by the auto-shrinkage of cement sheath (Lura, Jensen, & van Breugel, 2003), which can be determined by $\sigma_{ij}^{(2)} = 2G^v(\varepsilon_{ij} - \frac{1}{3}\delta_{ij}\varepsilon_0 + \frac{\nu^v}{1-2\nu^v}\delta_{ij}(\varepsilon - \varepsilon_0))$, where G^v rather than G^y is used because during the process when the shrinkage of the cement sheath being most prominent, the shear modulus is also smaller than that of the fully hydrated cement sheath (Boumiz, Vernet, & Tenoudji, 1996), ε_0 is volumetric auto-shrinkage of cement sheath. The initial stress of cement sheath σ_{ij}^0 can be expressed as follows

$$\sigma_{ij}^0 = \sigma_{ij}^{(1)} + \sigma_{ij}^{(2)} = 2G^v\left(\varepsilon_{ij} - \frac{1}{3}\delta_{ij}\varepsilon_0 + \frac{\nu^v}{1-2\nu^v}\delta_{ij}(\varepsilon - \varepsilon_0)\right) - \rho^{cem}gh\delta_{ij} \quad (44)$$

2.7. Failure criteria

Based on the real solutions in time domain shown in Section 2.5 and Mohr–Coulomb criterion, failure criteria for the three types of failure mode are developed to assess the safety of cement sheath. The strength criterion of cement sheath may be expressed by Terzaghi's effective stresses (Detournay & Cheng, 1988), which read

$$\begin{cases} \sigma'_{rr} = \sigma_{rr}^0 + \sigma_{rr} + p' \\ \sigma'_{\theta\theta} = \sigma_{\theta\theta}^0 + \sigma_{\theta\theta} + p' \end{cases} \quad (45)$$

where σ_{rr}^0 and $\sigma_{\theta\theta}^0$ are initial radial and hoop stress, respectively; $p' = p + p_0$ denotes the total pore pressure in porous material, p_0 is the initial pore pressure before loading, p is the pore water pressure generated during loading.

The shear failure of brittle material (e.g. cement paste or formation) is generally characterised by Mohr–Coulomb criterion. However, as argued by El Bitouri, Jamin, Pélissou, and El Yousoufi (2017), both cohesiveness coefficient coh and intrinsic friction angle φ in Mohr–Coulomb equation are temperature dependent, i.e. $coh(T_i), \varphi(T_i)$. Hence, failure takes place when the following equation is satisfied

$$\begin{cases} -\sigma'_{rr} \geq -\sigma'_{\theta\theta} \tan^2\left(\frac{\varphi(T_i)}{2} + \frac{\pi}{4}\right) + 2coh(T_i) \tan\left(\frac{\varphi(T_i)}{2} + \frac{\pi}{4}\right) \sigma'_{rr} \leq \sigma'_{\theta\theta} \leq \sigma_t \\ -\sigma'_{\theta\theta} \geq -\sigma'_{rr} \tan^2\left(\frac{\varphi(T_i)}{2} + \frac{\pi}{4}\right) + 2coh(T_i) \tan\left(\frac{\varphi(T_i)}{2} + \frac{\pi}{4}\right) \sigma'_{\theta\theta} \leq \sigma'_{rr} \leq \sigma_t \end{cases} \quad (46)$$

where σ_t is uniaxial tensile strength of the cement sheath and T_i denotes temperature of the material. The reason why minus signs appear in the equation lies in that the compressive stress is defined to be negative in this work, which is different from its general definition in the soil mechanics, compressive stress being positive.

Tensile failure occurs when $\sigma'_{rr} \geq \sigma_t$ or when $\sigma'_{\theta\theta} \geq \sigma_t$.

In addition to shear and tensile failures of cement sheath, a widespread failure mode is the debonding occurring at casing-cement sheath and cement sheath-formation interfaces. Such failure criterion can be expressed as

Table 1. Thermal, mechanical and geometrical properties of CCF system.

Material	Property	Value	Unit	Reference
Formation properties ^a	G_{for}^s	0.9	GPa	Abousleiman and Kanj (2004)
	K_{for}^s	3	GPa	Abousleiman and Kanj (2004)
	k_{for}^s	0.5×10^{-18}	m ²	Abousleiman and Kanj (2004)
	ϕ_0^{for}	0.1	1	Abousleiman and Kanj (2004)
Cement properties ^a	G_{cem}^s	10	GPa	Zhou, Dong, and Yang (2008)
	K_{cem}^s	21	GPa	Zhou et al. (2008)
	ϕ_0^{cem}	0.3	1	Zhou et al. (2008)
	k_{cem}^s	1×10^{-18}	m ²	Zhou et al. (2008)
	k_T^{cem}	0.34	W/m °C	Lienhard (2013)
	β^{cem}	3.00×10^{-5}	1/°C	Zhou et al. (2008)
Water properties	μ	1×10^{-3}	Pa · s	Abousleiman and Kanj (2004)
	K^f	2.18	GPa	Abousleiman and Kanj (2004)
	β_f	1.98×10^{-4}	1/°C	Lienhard (2013)
Casing properties	E^{cas}	200	GPa	Lienhard (2013)
	ν^{cas}	0.27	1	Lienhard (2013)
	k_T^{cas}	15	W/m °C	Lienhard (2013)
	β^{cas}	3.60×10^{-5}	1/°C	Lienhard (2013)
Geometry properties	r_1	0.10	m	–
	r_2	0.11	m	–
	r_3	0.16	m	–

^aHomogenised Poisson's ratio, bulk and shear modulus of formation and cement can be calculated with formulations in micromechanics (Dormieux et al., 2006; Yang, Lemarchand, Fen-Chong, & Azouni, 2015).

$$\sigma'_{rr} \geq [\sigma] \quad (47)$$

where $[\sigma]$ is the bonding strength of the interface.

In consequence, shear failure, tensile failure as well as the debonding at the interface can be well assessed if the stress state and the mechanical properties (i.e. cohesiveness, friction angle, tensile strength and bonding strength) of cement sheath are known.

3. Results and discussion

Similar to Xia et al. (2017), to focus on the variation of stress state in cement sheath after hydraulic and thermal loading, $\Delta_i \sigma_{\theta\theta}^{eff} = \sigma_{\theta\theta} + p$ and $\Delta_i \sigma_{rr}^{eff} = \sigma_{rr} + p$, referring to the variation of radial and hoop effective stresses after hydraulic (for $i=p$) and thermal (for $i=T$) loading, are used in the following analysis of this section. The thermal, mechanical and geometrical properties of casing, cement sheath and formation used in the following simulation are given in Table 1.

3.1. Influence of the hydraulic pressure in casing

The influence of the hydraulic pressure in casing (p_c) on the evolution of pore water pressure and effective stresses of cement sheath is discussed in this section. Herein, the temperature variation of cement sheath is zero and thus the thermal loading is not taken into account.

As illustrated in Figure 3, the pore water pressure at different radial displacement of the cement sheath exhibits a slight rise (i.e. more negative pressure) immediately after the exertion of hydraulic pressure in casing, before decreasing to zero due to the dissipation of pore water pressure. This is actually the Mandel–Cryer effect (Abousleiman & Kanj, 2004; Schiffman, Chen, & Jordan, 1969), which characterises the non-monotonic development of pore water pressure in cement sheath far away from the diffusing boundary (i.e. cement sheath-formation interface in

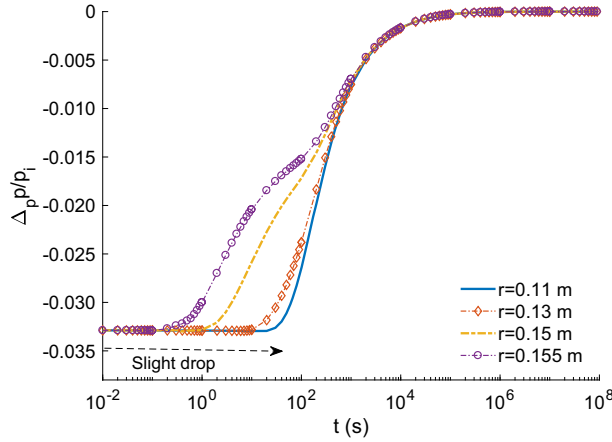


Figure 3. Evolution of pore pressure at different radial displacement of the cement sheath, p_i is the applied hydraulic pressure in casing and p denotes pore pressure generated after loading. It should be noted that, certain modification has been carried out for the pore pressure development at 0.155 m, detailed elaboration is given in Appendix B.

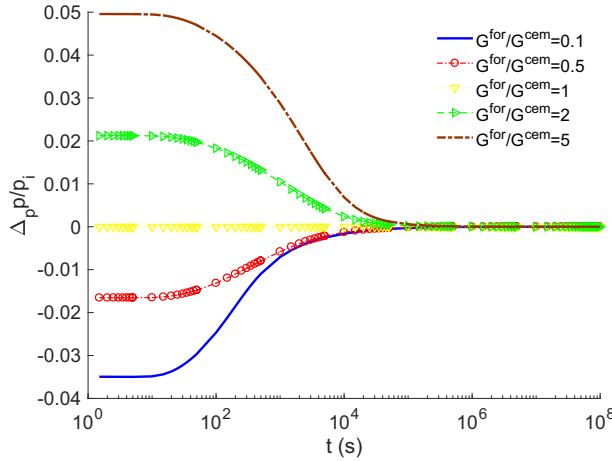


Figure 4. Evolution of pore pressure at $r=0.13$ m for different shear modulus ratios of formation to cement sheath, p_i is the applied hydraulic pressure in casing and p denotes pore pressure generated during loading, G^{for} varies with the ratios in the figure, other parameters (including G^{cem}) are given in Table 1.

this work). Figure 3 also shows that the rising trend lasts longer and reaches a higher magnitude at cement sheath-casing interface (i.e. $r=0.11$ m, the blue curve) because of the delayed pore water diffusion far away from the diffusing boundary. Moreover, a slight rise, here, indicates more negative pressure, which is different from the results in Abousleiman and Kanj (2004), where the slight rise corresponds to a more positive pressure. The reason for such difference lies in that the shear modulus of the cement sheath is higher than that of formation in this simulation (i.e. $G^{for}/G^{cem} = 0.14$), leading to instant negative pore pressure after loading (to be discussed later), unlike the positive one in Abousleiman and Kanj (2004) due to Skempton effect.

As depicted in Figure 4, the evolution of pore pressure with dissipating time is different when shear modulus ratio of formation to cement sheath G^{for}/G^{cem} varies. Pore water pressure remains zero when $G^{for} = G^{cem}$, the reason arises from that instantly the load is applied, the variation of porosity $\zeta = 0$ can be derived owing to instant q_f is 0 at $r < 0.16$ m; moreover, volumetric strain $\varepsilon = 0$ can also be obtained owing to the boundary conditions: $u_r(\infty) = 0$ and $\Delta T = 0$; $p = 0$ can, therefore, be

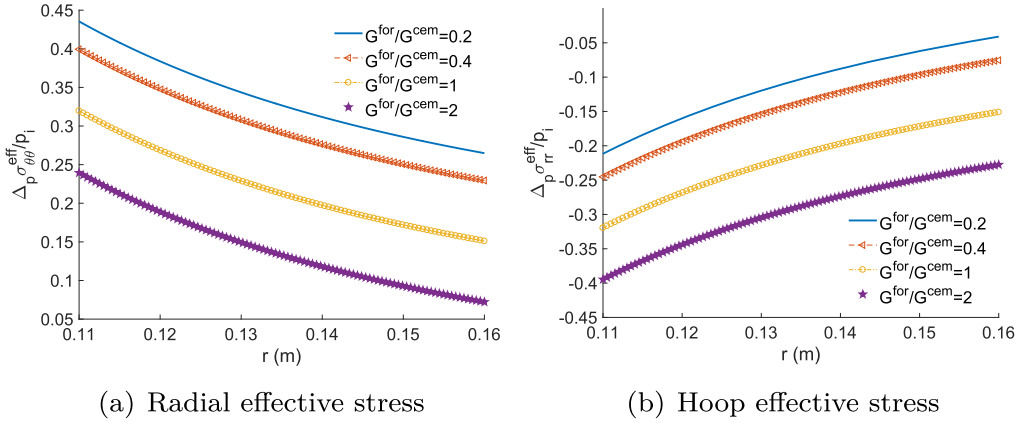


Figure 5. Influence of $G^{\text{for}}/G^{\text{cem}}$ on the distribution of radial effective stress (a) and hoop effective stress (b) of cement sheath at steady state ($t \rightarrow \infty$), G^{for} varies with the ratios in the figure, other parameters (including G^{cem}) are given in Table 1.

obtained according to Equation (2). When $G^{\text{for}} > G^{\text{cem}}$, i.e. cement sheath is softer than formation, the pore pressure remains positive before declining to zero. In this case, the confining effect of surrounding formation is more pronounced, resulting in more compressive radial stress and less tensile hoop stress; the body strain $\varepsilon = \varepsilon_{rr} + \varepsilon_{\theta\theta}$ becomes negative; since $\zeta = 0$, the pore pressure becomes positive according to Equation (2). When $G^{\text{for}} < G^{\text{cem}}$, the pore pressure remains negative before decreasing to zero; the reason for such phenomenon can be explained as the previous one. Furthermore, it can be found from Figures 3 and 4 that the pore water pressure in cement sheath arise from the hydraulic pressure p_i in casing is approximately two orders of magnitude less than p_i .

The influence of $G^{\text{for}}/G^{\text{cem}}$ on the variation of effective stress with radial displacement is illustrated in Figure 5. From the figure, it can be found that there exist the largest magnitude of radial (σ_{rr}^{eff}) and hoop ($\sigma_{\theta\theta}^{\text{eff}}$) effective stresses at the casing-cement sheath interface. It can also be found in the figure that the smaller the $G^{\text{for}}/G^{\text{cem}}$, the higher the hoop stress is. When $p_i = 50$ MPa, the variation of hoop effective stress can reach as high as 22 MPa as $G^{\text{for}}/G^{\text{cem}} = 0.2$, rendering tensile failure more likely to occur at the casing-cement sheath interface. This leads to the radial cracks in cement sheath initiating from the casing-cement sheath interface, which is in line with the finding of Wang and Taleghani (2014).

3.2. Influence of the thermal loading

In addition to the hydraulic pressure loading in casing, there is also thermal loading induced from the temperature difference between underground formation and injected water. When $p_i \neq 0$ and $\Delta T_0 = 0$ (ΔT_0 is the temperature difference between the injected water and the underground formation), according to the proposed model with the parameters in Table 1, $p/(\sigma_{rr} + p)$ can reach as much as 39.4%; while when $p_i = 0$ and $\Delta T_0 \neq 0$, $p/(\sigma_{rr} + p)$ can reach as much as 92.6%. Therefore, not only the pore pressure induced by the hydraulic pressure, but also the pore pressure brought about by thermal loading should be accounted for in the effective stress of cement sheath. For the convenience of discussion, $p_i = 0$ is assumed in this section.

Figure 6 shows the evolution of radial effective stress and hoop effective stress at different radial displacement owing to thermal loading. As can be found from Figure 6(a), immediately after applying thermal loading, a slight rise of the radial stress takes place, followed by a sharp drop to peak, after which, the radial stress reincreases to an equilibrium value. The slight rise of the radial stress can be explained as follows: at casing-cement sheath interface, the thermal loading ($\Delta T_0 < 0$) induces the tensile stress of cement sheath (positive) at $r > 0.11$ m instantly before the drop of the pore water pressure due to dissipation of pore water flux, which is similar to

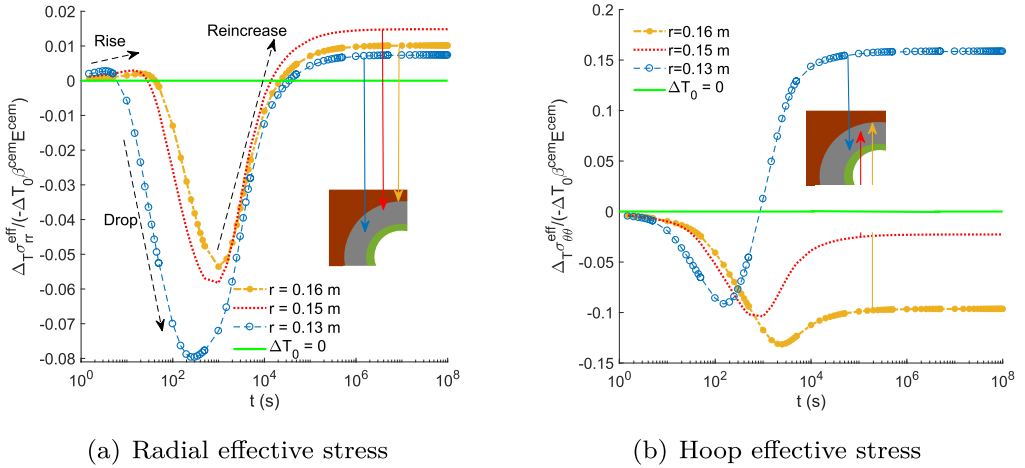


Figure 6. Evolution of radial (a) and hoop (b) effective stress at different location of cement sheath, $\Delta T_0 < 0$, $p_i = 0$, other parameters are given in Table 1.

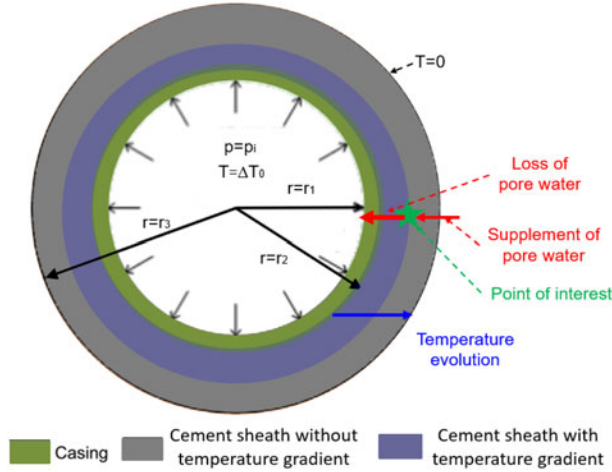


Figure 7. Illustration of temperature development and pore water fluid in cement sheath. Owing to the temperature drop in the blue region of cement sheath, loss of pore water from the point of interest is more significant than the supplement of it to the point, leading to a decrease in the pore water pressure at that point.

Mandel–Cryer effect; the sharp drop of the radial effective stress is attributed to the reduction of pore water pressure, resulting from the decrease of local temperature and the difference in thermal expansion coefficient between the solid phase of cement and the pore water; the reincrease of the radial effective stress arises from the supplement of pore water from the grey region of the cement sheath to the blue region (see Figure 7). The lack of slight rise of hoop effective stress in Figure 6(b) is due to the compressive hoop effective stress instead of tensile hoop effective stress at instant thermal loading. As can be also found in Figure 6(b), the hoop stress at $r=0.13$ m evolves from the compressive stress to tensile stress, the latter can reach as high as $0.16 \Delta T_0 \beta^{cem} E^{cem} \approx 2.4$ MPa ($\Delta T_0 = -100$ °C). As can also be found from Figure 6(a), at equilibrium state ($t \rightarrow \infty$), the radial effective stress at $r=0.15$ m (red dotted line) lies above the radial stresses at $r=0.16$ (yellow line) and $r=0.13$ (blue circle-dotted line), indicating that the maximum radial effective stress will occur within cement sheath instead of the casing-cement sheath interface and cement sheath-formation interface. This has also been found in Wang and

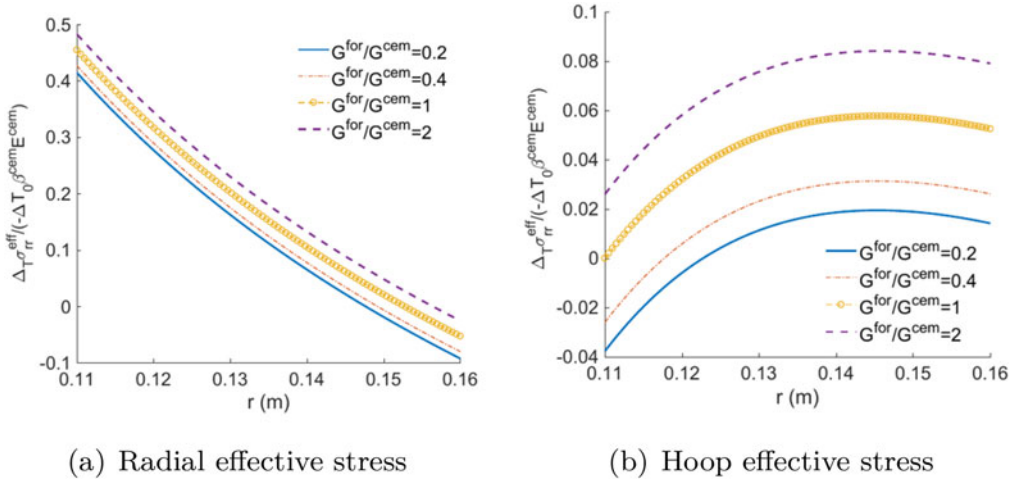


Figure 8. Impact of G_{for}/G_{cem} on the variation of radial (a) and hoop (b) effective stress with radial displacement at steady state ($t \rightarrow \infty$), $\Delta T_0 < 0$, $p_i = 0$, G^{for} varies with the ratios in the figure, other parameters (including G^{cem}) are given in Table 1.

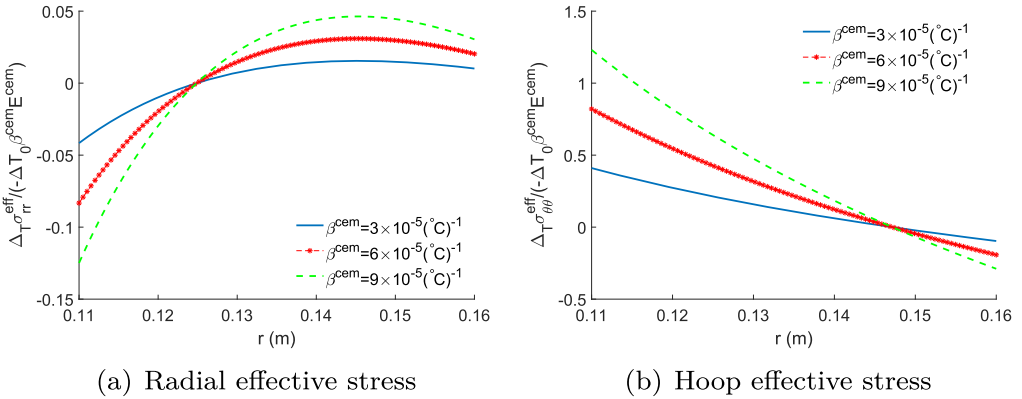


Figure 9. Influence of the thermal expansion coefficient of cement sheath on the variation of steady state ($t \rightarrow \infty$) radial (a) and hoop (b) effective stress with radial displacement at $t \rightarrow \infty$, $\Delta T_0 < 0$, $p_i = 0$, parameters other than β^{cem} are given in Table 1.

Dusseault (2003) when both pore water pressure and thermal stress are accounted for in porous formation.

Figure 8 plots the influence of G^{for}/G^{cem} on the variation of effective stress with radial displacement at $t \rightarrow \infty$ (i.e. at steady state). As illustrated in the figure, when $t \rightarrow \infty$, the stiffer the formation, the more tensile the effective stress is. This phenomenon indicates that the thermal loading induced by the difference between injected water and formation can offset the compressive stress induced by the hydraulic pressure in the casing (see Figure 5) as the formation becomes stiffer. However, it also increases the susceptibility of tensile failure in cement sheath at cement sheath-formation interface $r = 0.16$ m, that is to say, according to Figures 5(a) and 8(a), cement sheath-formation interface ($r = 0.16$ m) is susceptible to debonding; moreover, in terms of Figures 5(b) and 8(b), depending on the tensile strength of cement sheath and the magnitude of $\sigma_{\theta\theta}^{eff}$, the casing-cement sheath interface ($r = 0.11$ m) is highly susceptible to tensile failure and thus the occurrence of radial fracture, especially when taking initial pore water pressure into account.

Figure 9 depicts the impact of the thermal expansion coefficient of cement sheath on the variation of the hoop and radial effective stress of cement sheath with radial displacement.

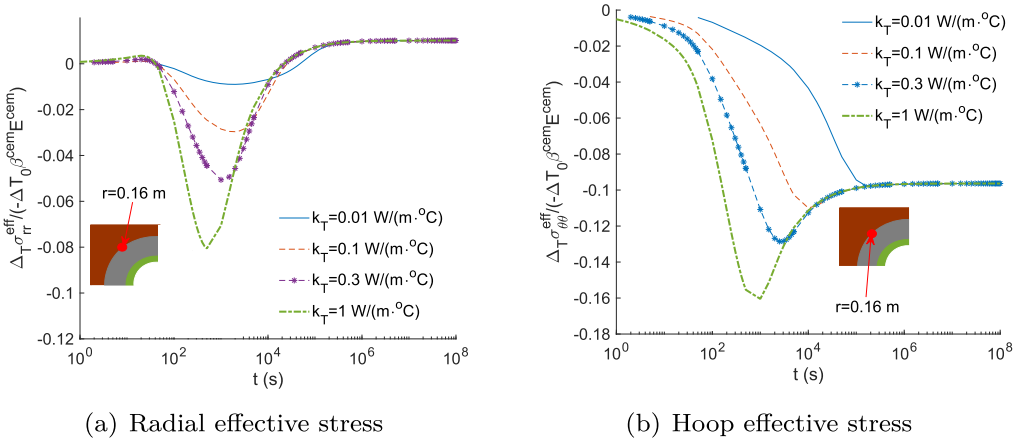


Figure 10. Impact of the thermal conductivity of cement sheath on the evolution of radial (a) and hoop (b) effective stress at $r=0.16$ m, $\Delta T_0 < 0$, $p_i = 0$, parameters other than k_T are given in Table 1.

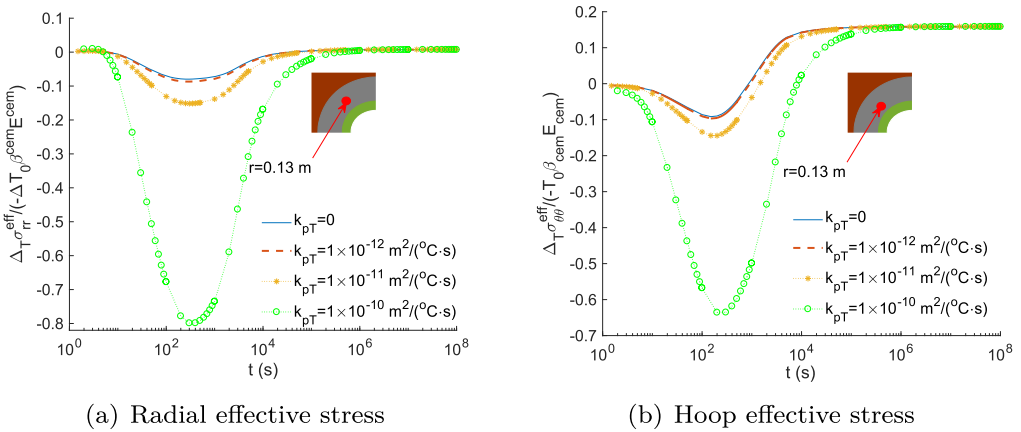


Figure 11. Influence of thermo-osmotic effect on the evolution of radial (a) and hoop (b) effective stress at $r=0.13$ m, $\Delta T_0 < 0$, $p_i = 0$, other parameters are given in Table 1.

As can be found from the figure, higher thermal expansion coefficient leads to more compressive radial effective stress at casing-cement sheath interface ($r=0.11$ m) and more tensile hoop effective stress at cement sheath-formation interface ($r=0.16$ m). It indicates that high thermal expansion coefficient of cement sheath results in a high susceptibility of tensile failure and, thus, an occurrence of radial fracture at cement sheath-formation interface ($r=0.16$ m).

Figure 10 illustrates the influence of the thermal conductivity of cement sheath on the evolution of radial effective stress and hoop effective stress. As shown in the figure, the higher the thermal conductivity, the greater both maximum radial and hoop effective stresses are and the earlier the peaks are reached. The reason for this phenomenon lies in that the faster the low temperature in casing spreads in the cement sheath, the more quickly the pore pressure would drop, leading to the earlier peak stress. Moreover, the more sudden drop of temperature in the cement sheath prevents an in time supplement of pore water, in turn, leading to more negative pore water pressure and higher compressive effective stress. Using the parameters in Table 1, the maximum compressive radial and hoop effective stresses in Figure 10 only become at most two times larger with k_T^{cem} increasing from 0.1 to 1. Moreover, thermal conductivity of cement

Table 2. Load scenarios.

Scenarios	ΔT_0 (°C)	p_i (MPa)
Scenario 1	−100	50
Scenario 2	−10	50

sheath can hardly vary that large. Therefore, the effect of the variation in thermal conductivity of cement sheath on its failure is negligible.

3.3. Influence of T-O effect

The influence of the T-O effect on the evolution of the effective stress at $r=0.13$ m is depicted in Figure 11. As can be found in the figure, both radial and hoop effective stresses becomes more and more compressive with increasing T-O coefficient k_{pT} . This can be explained according to Equations (12) and (15): higher T-O coefficient makes the loss of pore water at $r=0.13$ m (i.e. the green star in Figure 7) towards the inner part of cement sheath (the blue ring) faster than the supplement of pore water from the outer part (i.e. the grey ring) of cement sheath, where the temperature gradient is absent owing to delayed heat transfer and thus the pore water flux is merely induced from pressure gradient. Therefore, such non-equilibrium process at $r=0.13$ m, i.e. loss of pore water being greater than supplement of pore water, results in the sharp drop of pore pressure.

As illustrated in Figure 11, when T-O coefficient $k_{pT} \leq 1 \times 10^{-12} \text{ m}^2/(\text{°Cs})$, the influence of the T-O effect on the evolution of the effective stress is negligible; however, when $k_{pT} \geq 1 \times 10^{-12} \text{ m}^2/(\text{°Cs})$, the influence of the T-O effect on the evolution of the effective stress becomes more and more significant with increase of k_{pT} . Recalling discussions about T-O coefficient of cement sheath in Section 2.2, when the water cement ratio of cement sheath is low, the T-O coefficient of cement sheath, which can be as high as $1 \times 10^{-10} \text{ m}^2/(\text{°Cs})$, leads to a maximum compressive radial and hoop effective stress several orders of magnitude larger than the case when T-O coefficient is neglected (see Figure 11). On the contrary, for cement with large ratio of water to cement, which results in $k_{pT} \leq 1 \times 10^{-12} \text{ m}^2/(\text{°Cs})$, T-O effect can be neglected (see Figure 11).

3.4. Parametric sensitivity analyses

In the preceding sections, the influence of poroelastic effect ($p_i \neq 0, \Delta T_0 = 0$ and $k_{pT} = 0$), thermal loading ($p_i = 0, \Delta T_0 \neq 0$ and $k_{pT} = 0$) and T-O effect ($p_i = 0, \Delta T_0 \neq 0$ and $k_{pT} \neq 0$) on the evolution of effective stress of cement sheath is discussed, respectively. All the three effects can thus be coupled into a comprehensive thermo-poroelastic model for cement sheath. Comprehensive parametric sensitivity analyses are carried out to figure out which parameters are more critical to the integrity of cement sheath, which will be helpful in cement sheath preparation.

The influence of poroelastic, thermal and T-O properties of the cement sheath: thermal expansion coefficient β^{cem} , thermal conductivity k_T , T-O coefficient k_{pT} , shear modulus ratio of formation to cement sheath G^{for}/G^{cem} , intrinsic permeability k^{cem} , initial porosity ϕ_0^{cem} , shear modulus of the solid phase in cement sheath $G^{s,cem}$, as well as bulk modulus of the solid phase in cement sheath $K^{s,cem}$, on maximum radial compressive effective stress and hoop tensile effective stress of cement sheath is discussed. Since the temperature difference between injected water and formation influences the relative importance of thermal and mechanical behaviours of cement sheath, parameters are compared under two load scenarios shown in Table 2. Through time (0 to 10^8 s) and radial displacement ($0.11 \text{ m} \leq r \leq 0.16 \text{ m}$) discretization, the maximum radial compressive effective stress and hoop tensile effective stress in cement sheath are determined in

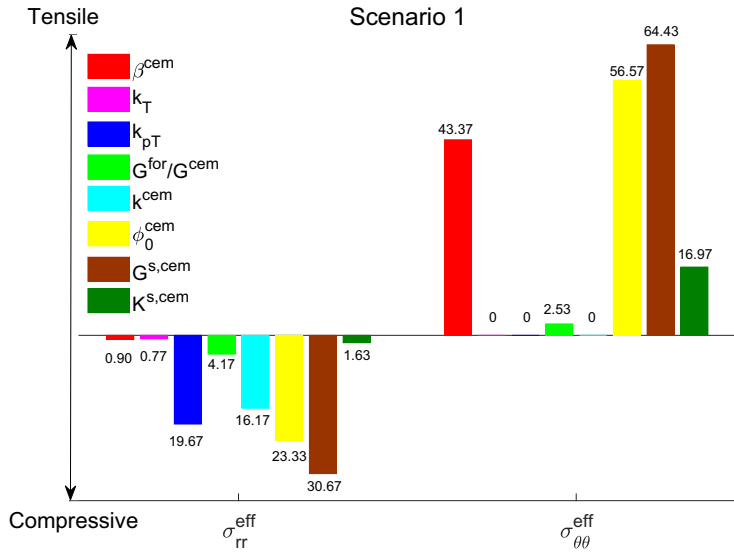


Figure 12. Sensitivity analyses of the maximum hoop and radial effective stress of cement sheath with respect to the variation of poromechanical, thermal and thermo-osmotic properties in Scenario 1 (S1), the unit of labelled numbers is %.

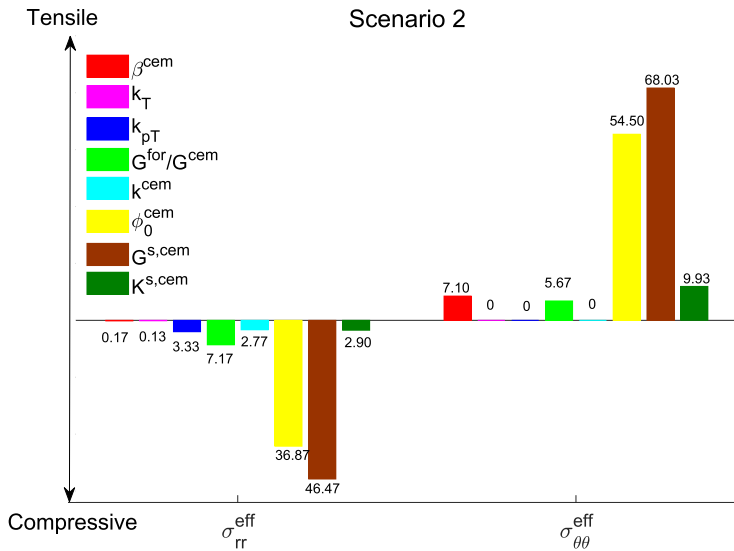


Figure 13. Sensitivity analyses of the maximum hoop and radial effective stress of cement sheath with respect to the variation of poromechanical, thermal and thermo-osmotic properties in Scenario 2 (S2), the unit of labelled numbers is %.

both temporal and spatial dimensions. In the parametric analysis, one of the eight parameters is taken as 30% greater than that shown in Table 1 while other seven parameters remain the same as in Table 1. The maximum compressive stress is designated to reflect the change of radial effective stress, while the maximum tensile stress is designated as the reflection of variation of hoop effective stress. Herein, dimensionless variations of both radial and hoop effective stresses are expressed as $\frac{\Delta\sigma_{ii}^{eff}}{\Delta x/x}$ ($i = \theta$ or $i = r$) (García-Macías, D'Alessandro, Castro-Triguero, Pérez-Mira, & Ubertaini, 2017), where x can be any of the eight parameters, $\Delta\sigma_{ii}^{eff}$ is variation of radial ($i = r$) or hoop ($i = \theta$) effective stresses; Δx is variation of x .

Table 3. Parameters used in failure criteria (El Bitouri et al., 2017).

	Value1	Value2	Unit
T_0^{cem}	20	120	°C
c_{oh}	4.1	1.1	MPa
ϕ	47.6	23.5	°
σ_t	2.1	0.2	MPa

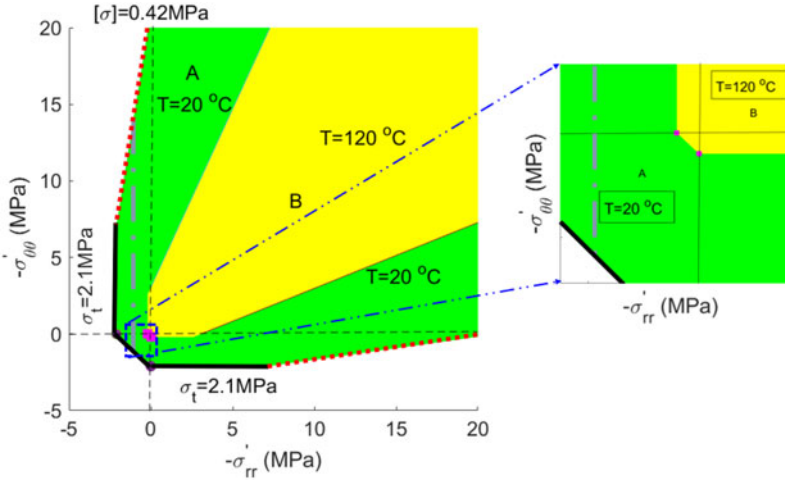


Figure 14. Failure envelopes of cement sheath. The yellow domain B is safety domain under 120°C, while domain $A \cup B$ is safety domain under 20°C. The black solid lines, red dotted lines and grey dash-dotted lines denote envelopes of tensile failures, shear failures of cement sheath, and debonding at casing-cement sheath or cement sheath-formation interfaces, respectively.

As illustrated in Figures 12 and 13, among eight parameters, ϕ_0^{cem} and $G^{s,cem}$ have the most significant influence on the effective stress in both scenarios, and thus are critical parameters in cement sheath design. On the contrary, the influence of both k_T and G^{for}/G^{cem} is negligible ($<10\%$). The influence of thermal properties (i.e. β^{cem} and k_{pT}), k^{cem} and $K^{s,cem}$ of cement sheath, is more pronounced at higher thermal loading, i.e. $\Delta T_0 = -100^\circ\text{C}$ in S1 loading. More specifically, at high thermal loading scenario, corresponding to deep oil well exploitation, k_{pT} and k^{cem} are more important for the compressive radial effective stress, while β^{cem} and $K^{s,cem}$ play more important roles in tensile hoop effective stress. β^{cem} and $K^{s,cem}$ are closely related to the radial cracking in cement sheath, and thus both of them are of great significance in cement sheath design.

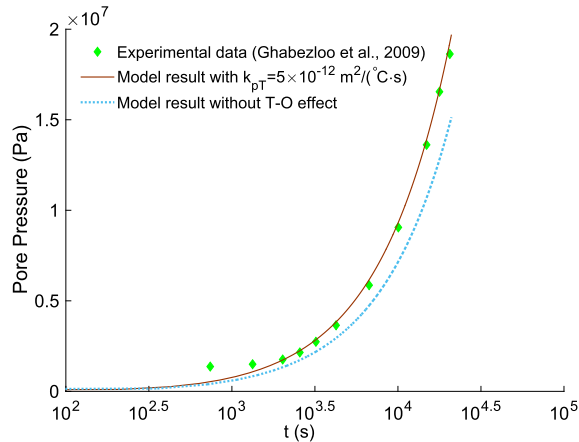
3.5. Failure envelopes of cement sheath

On the premise of the failure criteria developed in Section 3.5 and the parameters given in Table 3, the allowable effective stresses inside cement sheath (excluding interface) at $T_0^{cem} = 20^\circ\text{C}$ and $T_0^{cem} = 120^\circ\text{C}$ are respectively plotted as green (defined as domain A) + yellow domain (defined as domain B) and yellow domain in Figure 14. As can be found, there is a significant shrinkage in area from domain $A \cup B$ to domain B when temperature increases from 20°C to 120°C , indicating that the cement sheath is more susceptible to both shear and tensile failures under higher temperature.

When it comes to the casing-cement sheath and cement sheath-formation interfaces, the safety zone would be different from that at the inner part of cement sheath. Assuming that

Table 4. Thermal and poromechanical properties of oil cement sample (Ghabezloo et al., 2009).

Properties	K^c	G^s	K^f	β_l	β_s	k	ϕ_0
Values	21	5.2	2.27	3.5×10^{-4}	9.6×10^{-5}	1.1×10^{-19}	0.26
Unit	GPa	GPa	GPa	$(^\circ\text{C})^{-1}$	$(^\circ\text{C})^{-1}$	m^2	–

**Figure 15.** Evolution of pore water pressure within oil cement sample in a triaxial undrained test subjected to a uniform temperature, the experiment data are after Ghabezloo et al. (2009).**Table 5.** Parameters used in case study.

	Meaning of symbols	Value	Unit
coh	Cohesiveness coefficient	19.2	MPa
ϕ	Intrinsic friction angle	17.8	$^\circ$
σ_t	Tensile strength	4.0	MPa
ε_0	Volumetric shrinkage	1×10^{-3}	1
ρ^{cem}	Density of cement sheath	2.2×10^3	kg/m^3
p_0	Initial pore pressure	$0.005h^a$	MPa
p_i	Hydraulic pressure	$50 + 0.01h^a$	MPa

^aThe unit of h is m.

bonding strengths at both interfaces are 1 MPa at 20°C, such difference is demonstrated in Figure 14.

4. Model validation and a case study

4.1. Model validation

Until now, there are scarce experimental data, either in-lab ones or field ones, on thermo-poroelastic response of the cement sheath in CCF system. As an alternative, the proposed thermo-poroelastic model is validated by the experimental data of Ghabezloo, Sulem, and Saint-Marc (2009), i.e. the evolution of the pore pressure induced by thermal loading in triaxial experiment of undrained oil well cement paste. In the experiment conducted by Ghabezloo et al. (2009), the oil cement paste sample is a cylindrical paste with a diameter of 38 mm and a length of 76 mm. The sample is undrained and the boundary of which is exerted a zero confining pressure as well as a uniform thermal loading, which increases from 18°C to 87°C at a rate of 0.1°C/min (Ghabezloo et al., 2009). The evolution of the pore pressure with time is simultaneously measured during the thermal loading. The thermal and poromechanical properties of cylindrical oil cement are given in Table 4.

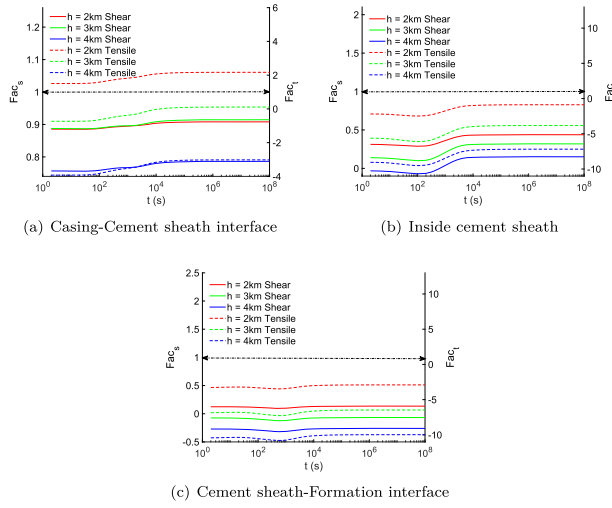


Figure 16. The evolutions of FAC_s and FAC_t at different depths of the CCF system, among which (a) is the casing-cement sheath interface, (b) is a point inside cement sheath and (c) is the cement sheath-formation interface.

Though boundary conditions of the triaxial undrained test are different from that of the CCF system in this work, thermo-poroelastic model still works for the oil cement sample subjected to a uniform thermal loading. With the boundary conditions of the triaxial undrained test, i.e. zero confining pressure and uniform thermal loading, as well as assigning $r_2 \rightarrow 0$ and $r_3 = 0.019$ m in the expressions of C_1 – C_6 , the constants C_1 – C_6 in Equations (29)–(36) can thus be determined. The simulated pore pressures with dissipating time with and without T-O effect are plotted with experimental data in Figure 15. As can be found from the figure, pronounced discrepancies exist between the model results without T-O effect and the experimental data; however, the model result with $k_{pT} = 5 \times 10^{-12} \text{m}^2/(\text{°Cs})$ well reproduces the experimental results.

4.2. A case study

The pore pressure of cement sheath, the thermal stress induced by the temperature difference and the accompanied heat conduction and T-O effects, and initial stress of cement sheath are fully accounted for in this case study. In addition to the parameters given in Tables 1 and 5, $G^{cem'} = 0.5G^{cem}$ (see Equation (44)) and the initial distribution of underground formation temperature in Equation (48) is adopted from Tian, Shi, and Qiao (2015)

$$\begin{cases} \Delta T_0 = 0.025h & h \leq 3000 \\ \Delta T_0 = 75 & h > 3000 \end{cases} \quad (48)$$

On premise of Equation (46), the tendencies of shear and tensile failure of cement sheath are assessed by the following two dangerous factors:

$$\begin{cases} FAC_s = \frac{-\sigma'_{rr} + \sigma'_{\theta\theta} \tan^2\left(\frac{\varphi}{2} + \frac{\pi}{4}\right)}{2coh \tan\left(\frac{\varphi}{2} + \frac{\pi}{4}\right)} \\ FAC_t = \frac{\max\{\sigma'_{rr}, \sigma'_{\theta\theta}\}}{\sigma_t} \end{cases} \quad (49)$$

in which Fac_s or Fac_t are shear failure and tensile failure dangerous factors, respectively, they will be greater than 1 when shear or tensile failure occurs in cement sheath.

The evolutions of shear (Fac_s) and tensile (Fac_t) dangerous factors with dissipating time at different depths of underground and at different locations of the cement sheath are illustrated in Figure 16. As plotted in Figure 16(a–c), owing to the coupling of the pore pressure and thermal effect, cement sheath is more and more apt to occurrence of shear and tensile failure with dissipating time, which is more pronounced after 10^4 s, this can be explained by the thermal effect and the Mandel–Cryer effect induced by the pore pressure. Comparing Figure 16(a–c), it can also be found that the casing-cement sheath interface is always more likely to lose integrity at different depths of underground formation, the cement sheath is expected to be tensile failure at the depth of 2000 m, which is in line with the argument proposed by Wang and Taleghani (2014). Moreover, Figure 16(a–c) also show that shear and tensile failure of cement sheath tends to initiate from the position closer to the ground surface, this is because in vicinity of ground surface, initial tensile stress arose from auto-shrinkage prevails over the initial compressive stress brought about by the hydraulic pressure by the cement slurry.

5. Concluding remarks

A comprehensive thermo-poroelastic model for cement sheath in CCF system, accounting for hydraulic pressure in casing, thermal loading induced by temperature difference between underground formation and injected water, and T-O effect, is developed in this work. Moreover, failure criteria, whose parameters are temperature dependent, are proposed to assess the failure of cement sheath. The influence of the hydraulic pressure in casing, thermal loading and thermal-osmotic effect is discussed in this work. Parametric sensitivity analyses are carried out to assess the potential randomness of the input parameters on the overall evolution of effective stress. Several conclusions can be drawn:

1. When both thermal loading and thermal-osmotic effect are disregarded, the pore water pressure in cement sheath induced by the hydraulic pressure p_i in casing is approximately two orders of magnitude less than p_i . Moreover, shear modulus ratio of formation to cement sheath G^{for}/G^{cem} plays a significant role in the evolution of pore water pressure with dissipating time: when $G^{for} = G^{cem}$, pore pressure remains zero; when $G^{for} > G^{cem}$, i.e. cement sheath is softer than formation, pore water pressure remains positive before declining to zero; when $G^{for} < G^{cem}$, the pore pressure maintains negative before decreasing to zero. The stiffer the cement sheath, the higher the potential for the occurrence of the radial fracture of cement sheath exists owing to the hydraulic pressure in casing.
2. When both hydraulic pressure in casing and thermal-osmotic effect are disregarded, the magnitude of the pore water pressure arising from thermal loading is significantly greater than that of the total radial and hoop thermal stress. It is found that higher G^{for}/G^{cem} and higher volumetric thermal dilation coefficient of cement sheath β^{cem} lead to a higher risk of radial fracture initiated at the casing-cement sheath interface, as well as a greater susceptibility to debonding at casing-cement sheath interface, especially when taking initial pore water pressure p_0 into account; whereas, thermal conductivity of cement sheath k_T plays a negligible role in evolution of effective stress, and thus has subtle influence on the failure of cement sheath.
3. The influence of the T-O effect on the evolution of effective stress of cement sheath is accounted for in this work. When T-O coefficient $k_{pT} \leq 1 \times 10^{-12} \text{ m}^2/(\text{°Cs})$, the influence of the T-O effect on the evolution of the effective stress is negligible; however, when $k_{pT} \geq 1 \times 10^{-12} \text{ m}^2/(\text{°Cs})$, the influence of the T-O effect on the evolution of the effective stress becomes more significant with increase of k_{pT} .

4. The parametric sensitivity analyses show that initial porosity of cement sheath ϕ_0^{cem} and shear modulus of the solid phase in cement sheath $G^{s,cem}$ have the most significant influence on evolution of the effective stress of cement sheath and should be paid special attention to in the design of cement sheath. Moreover, in high thermal loading scenario ($\Delta T_0 = -100^\circ\text{C}$ and $p_i = 50\text{ MPa}$), thermal expansion coefficient β^{cem} , bulk modulus of the solid phase of cement sheath $K^{s,cem}$, T-O coefficient k_{pT} and intrinsic permeability of cement sheath k^{cem} are also important in the design of cement sheath. β^{cem} and $K^{s,cem}$ are closely related to tensile hoop effective stress and thus are crucial to the initiation of radial cracking in cement sheath.
5. The application of the proposed model on a triaxial test of undrained heating of oil well cement paste shows that the model with $k_{pT} = 5 \times 10^{-12} \text{ m}^2/(\text{°C s})$ well reproduces the experimental results.
6. The case study shows that casing-cement sheath interface is susceptible to shear and tensile failures, moreover, when the CCF system is closer to ground surface, it is apt to occurrence of shear and tensile failure.

The proposed model is envisaged to provide a useful tool for analysing the effective stress of cement sheath and, therefore, is valuable for the quantitative design of cement sheath used in shale gas exploitation. In addition, the proposed model is expected to be useful in analysing thermo-poroelastic behaviours of cement sheath in geothermal drilling and nuclear waste repository sealing.

Acknowledgments

The authors are grateful to Professor E. Detournay at the University of Minnesota for his support during the course of this work. This study was supported by grants from the National Natural Science Foundation of China (NSFC) project (Grant no. 51708404).

Disclosure statement

No potential conflict of interest was reported by the authors.

Funding

This study was supported by grant from the National Natural Science Foundation of China (NSFC) project (grant no. 51708404).

ORCID

Rongwei Yang  <http://orcid.org/0000-0002-3991-426X>

References

- Abousleiman, Y. N., & Kanj, M. Y. (2004). The generalized Lamé problem—Part II: Applications in poromechanics. *Journal of Applied Mechanics*, 71(2), 180–189. doi:10.1115/1.1683800
- Ardakani, S. M., & Ulm, F. J. (2013). Chemoelastic fracture mechanics model for cement sheath integrity. *Journal of Engineering Mechanics*, 140(4), 04013009. doi:10.1061/(ASCE)EM.1943-7889.0000690
- Boumiz, A., Vernet, C., & Tenoudji, F. C. (1996). Mechanical properties of cement pastes and mortars at early ages: Evolution with time and degree of hydration. *Advanced Cement Based Materials*, 3, 94–106. doi:10.1016/S1065-7355(96)90042-5

- Carnahan, C. (1983). Thermodynamic coupling of heat and matter flows in near-field regions of nuclear waste repositories. *MRS Online Proceedings Library Archive*, 26, 1023–1030.
- Cheng, A. H. D. (2016). *Poroelectricity* (Vol. 27). Cham: Springer.
- De Andrade, J., & Sangesland, S. (2016). Cement sheath failure mechanisms: Numerical estimates to design for long-term well integrity. *Journal of Petroleum Science and Engineering*, 147, 682–698. doi:10.1016/j.petrol.2016.08.032
- Derjaguin, B., & Sidorenkov, G. (1941). Thermoosmosis at ordinary temperatures and its analogy with the thermo-mechanical effect in helium II. *Comptes Rendus de l'Académie des Sciences*, 32, 622–626.
- Detournay, E., & Cheng, A. D. (1988). Poroelectric response of a borehole in a non-hydrostatic stress field. *International Journal of Rock Mechanics and Mining Sciences & Geomechanics Abstracts*, 25, 171–182. doi:10.1016/0148-9062(88)92299-1
- Dormieux, L., Kondo, D., & Ulm, F. J. (2006). *Microporomechanics*. New York, NY: Wiley.
- El Bitouri, Y., Jamin, F., Pélioussou, C., & El Youssoufi, M. (2017). Tensile and shear bond strength between cement paste and aggregate subjected to high temperature. *Materials and Structures*, 50(6), 234. doi:10.1617/s11527-017-1105-8
- Falser, S., Uchida, S., Palmer, A., Soga, K., & Tan, T. (2012). Increased gas production from hydrates by combining depressurization with heating of the wellbore. *Energy & Fuels*, 26, 6259–6267. doi:10.1021/ef3010652
- Gao, J., Deng, J., Lan, K., Song, Z., Feng, Y., & Chang, L. (2017). A porothermoelastic solution for the inclined borehole in a transversely isotropic medium subjected to thermal osmosis and thermal filtration effects. *Geothermics*, 67, 114–134. doi:10.1016/j.geothermics.2017.01.003
- Gao, Y., Liu, Z., Zhuang, Z., Hwang, K. C., Wang, Y., Yang, L., & Yang, H. (2016). Cylindrical borehole failure in a poroelectric medium. *Journal of Applied Mechanics*, 83(6), 061005. doi:10.1115/1.4032859
- García-Macías, E., D'Alessandro, A., Castro-Triguero, R., Pérez-Mira, D., & Ubertini, F. (2017). Micromechanics modeling of the electrical conductivity of carbon nanotube cement-matrix composites. *Composites Part B: Engineering*, 108, 451–469. doi:10.1016/j.compositesb.2016.10.025
- Gelet, R., Loret, B., & Khalili, N. (2012). Borehole stability analysis in a thermoporoelectric dual-porosity medium. *International Journal of Rock Mechanics and Mining Sciences*, 50, 65–76. doi:10.1016/j.ijrmms.2011.12.003
- Ghabezloo, S., Sulem, J., & Saint-Marc, J. (2009). The effect of undrained heating on a fluid-saturated hardened cement paste. *Cement and Concrete Research*, 39(1), 54–64. doi:10.1016/j.cemconres.2008.09.004
- Ghassemi, A., Tao, Q., & Diek, A. (2009). Influence of coupled chemo-poro-thermoelastic processes on pore pressure and stress distributions around a wellbore in swelling shale. *Journal of Petroleum Science and Engineering*, 67(1–2), 57–64. doi:10.1016/j.petrol.2009.02.015
- Gonçalvès, J., Ji Yu, C., Matray, J. M., & Tremosa, J. (2018). Analytical expressions for thermo-osmotic permeability of clays. *Geophysical Research Letters*, 45(2), 691–698. doi:10.1002/2017GL075904
- Gonçalvès, J., & Trémosa, J. (2010). Estimating thermo-osmotic coefficients in clay-rocks: I. Theoretical insights. *Journal of Colloid and Interface Science*, 342(1), 166–174. doi:10.1016/j.jcis.2009.09.056
- Kanfar, M. F., Chen, Z., & Rahman, S. (2017). Analyzing wellbore stability in chemically-active anisotropic formations under thermal, hydraulic, mechanical and chemical loadings. *Journal of Natural Gas Science and Engineering*, 41, 93–111. doi:10.1016/j.jngse.2017.02.006
- Kim, S., & Mench, M. (2009). Investigation of temperature-driven water transport in polymer electrolyte fuel cell: Thermo-osmosis in membranes. *Journal of Membrane Science*, 328(1–2), 113–120. doi:10.1016/j.memsci.2008.11.043
- Kurashige, M. (1992). Thermal stresses of a fluid-saturated poroelectric hollow cylinder. *JSME International Journal. Ser. 1, Solid Mechanics, Strength of Materials*, 35(4), 386–391. doi:10.1299/jsmea1988.35.4_386
- Lavrov, A., & Torsæter, M. (2016). *Physics and mechanics of primary well cementing*. Cham: Springer.
- Lienhard, J. H. (2013). *A heat transfer textbook*. North Chelmsford, MA: Courier Corporation.
- Loh, M., Too, J. L., Falser, S., Linga, P., Khoo, B. C., & Palmer, A. (2014). Gas production from methane hydrates in a dual wellbore system. *Energy & Fuels*, 29, 35–42. doi:10.1021/ef501769r
- Lura, P., Jensen, O. M., & van Breugel, K. (2003). Autogenous shrinkage in high-performance cement paste: An evaluation of basic mechanisms. *Cement and Concrete Research*, 33(2), 223–232. doi:10.1016/S0008-8846(02)00890-6
- Petersen, T. A. (2015). *Chemo-poro-elastic fracture mechanics of wellbore cement liners: The role of eigenstress and pore pressure on the risk of fracture* (Ph.D. thesis), Massachusetts Institute of Technology, Cambridge, MA.
- Schiffman, R. L., Chen, A., & Jordan, J. C. (1969). An analysis of consolidation theories. *Journal of Soil Mechanics & Foundations Div*, 95, 285–312.
- Shi, Y., Li, B., Guo, B., Guan, Z., & Li, H. (2015). An analytical solution to stress state of casing-cement sheath-formation system with the consideration of its initial loaded state and wellbore temperature variation. *International Journal of Emerging Technology and Advanced Engineering*, 5, 59–65.
- Stehfest, H. (1970). Algorithm 368: Numerical inversion of Laplace transforms [D5]. *Communications of the ACM*, 13(1), 47–49. doi:10.1145/361953.361969
- Tian, Z., Shi, L., & Qiao, L. (2015). Research of and countermeasure for wellbore integrity of shale gas horizontal well. *Natural Gas Industry*, 35, 70–76.
- Trémosa, J., Gonçalvès, J., Matray, J., & Violette, S. (2010). Estimating thermo-osmotic coefficients in clay-rocks: II. In situ experimental approach. *Journal of Colloid and Interface Science*, 342(1), 175–184. doi:10.1016/j.jcis.2009.09.055

- Wang, L., Bornert, M., Héripré, E., Chanchole, S., Pouya, A., & Halphen, B. (2015). Microscale insight into the influence of humidity on the mechanical behavior of mudstones. *Journal of Geophysical Research: Solid Earth*, 120, 3173–3186. doi:10.1002/2015JB011953
- Wang, L., Pouya, A., Bornert, M., & Halphen, B. (2014). Modelling the internal stress field in argillaceous rocks under humidification/desiccation. *International Journal for Numerical and Analytical Methods in Geomechanics*, 38(16), 1664–1682. doi:10.1002/nag.2267
- Wang, W., & Taleghani, A. D. (2014). Three-dimensional analysis of cement sheath integrity around wellbores. *Journal of Petroleum Science and Engineering*, 121, 38–51. doi:10.1016/j.petrol.2014.05.024
- Wang, Y., & Dusseault, M. B. (2003). A coupled conductive–convective thermo-poroelastic solution and implications for wellbore stability. *Journal of Petroleum Science and Engineering*, 38(3–4), 187–198. doi:10.1016/S0920-4105(03)00032-9
- Xia, Y., Jin, Y., Chen, M., & Lu, Y. (2017). Dynamic analysis of a cylindrical casing–cement structure in a poroelastic stratum. *International Journal for Numerical and Analytical Methods in Geomechanics*, 41(12), 1362–1389. doi:10.1002/nag.2680
- Yang, R., Gui, Q., Lemarchand, E., Fen-Chong, T., & Li, K. (2015). Micromechanical modeling of transport properties of cement-based composites: Role of interfacial transition zone and air voids. *Transport in Porous Media*, 110(3), 591–611. doi:10.1007/s11242-015-0574-x
- Yang, R., Lemarchand, E., & Fen-Chong, T. (2016). A micromechanics model for solute diffusion coefficient in unsaturated granular materials. *Transport in Porous Media*, 111(2), 347–368. doi:10.1007/s11242-015-0597-3
- Yang, R., Lemarchand, E., Fen-Chong, T., & Azouni, A. (2015). A micromechanics model for partial freezing in porous media. *International Journal of Solids and Structures*, 75, 109–121. doi:10.1016/j.ijsolstr.2015.08.005
- Yang, R., Li, K., Lemarchand, E., & Fen-Chong, T. (2016). Micromechanics modeling the solute diffusivity of unsaturated granular materials. *International Journal of Multiphase Flow*, 79, 1–9. doi:10.1016/j.ijmultiphaseflow.2015.10.004
- Zhang, Z., & Wang, H. (2017). Effect of thermal expansion annulus pressure on cement sheath mechanical integrity in hpht gas wells. *Applied Thermal Engineering*, 118, 600–611. doi:10.1016/j.applthermaleng.2017.02.075
- Zheng, L., & Samper, J. (2008). A coupled THMC model of FEBEX mock-up test. *Physics and Chemistry of the Earth, Parts A/B/C*, 33, S486–S498. doi:10.1016/j.pce.2008.10.023
- Zhou, S., Dong, Y., & Yang, H. (2008). Thermal dilation coefficients of several hardened cement pastes (in Chinese). *Journal of Yangtze River Scientific Research Institute*, 25, 70–72.
- Zimmerman, R. (2000). Coupling in poroelasticity and thermoelasticity. *International Journal of Rock Mechanics and Mining Sciences*, 37(1–2), 79–87. doi:10.1016/S1365-1609(99)00094-5

Appendix A. Details on general solutions for governing equations

1. Solutions for casing

It is yielded from Equations (1), (4) and (5) that

$$\varepsilon^{\circ} = F_1 \quad (\text{A.1})$$

$$u_r^{\circ} = \frac{r}{2} F_1 + \frac{F_2}{r} \quad (\text{A.2})$$

Considering that under axial symmetric geometry, we have

$$\varepsilon_{rr}^{\circ} = \frac{\partial u_r^{\circ}}{\partial r} \quad (\text{A.3})$$

$$\varepsilon_{\theta\theta}^{\circ} = \frac{u_r^{\circ}}{r} \quad (\text{A.4})$$

$$\varepsilon^{\circ} = \varepsilon_{rr}^{\circ} + \varepsilon_{\theta\theta}^{\circ} \quad (\text{A.5})$$

Therefore,

$$\varepsilon_{rr}^{\circ} = \frac{F_1}{2} - \frac{F_2}{r^2} \quad (\text{A.6})$$

Then, substituting Equations (A.1) and (A.6) into (1) yields

$$\sigma_{rr}^{\circ} = 2G \left(\varepsilon_{rr}^{\circ} - \frac{1}{3} \beta \Delta T_0 + \frac{\nu}{1-2\nu} (\varepsilon^{\circ} - \beta \Delta T_0) \right) \quad (\text{A.7})$$

2. Solutions for cement sheath

In order to solve Equation (27), all the variables are to be transformed into the Laplace domain,

$$\begin{cases} s \Delta T^{\circ} - \kappa_T \nabla^2 (\Delta T^{\circ}) = 0 \\ s p^{\circ} - c \nabla^2 p^{\circ} = s c_T \Delta T^{\circ} - s c_g g^{\circ} \end{cases} \quad (\text{A.8})$$

where g° is actually a constant in Laplace domain, and that

$$c_T = \frac{\beta_c + \frac{k_{pT}}{\kappa_T}}{S} \quad (\text{A.9})$$

$$c_g = \frac{\alpha}{S} \quad (\text{A.10})$$

First, we could get the solution for temperature from the first equation in (A.8) independently.

$$\Delta T^{\circ} = C_1 I_0(\xi_T) + C_2 K_0(\xi_T) \quad (\text{A.11})$$

where $\xi_T = \sqrt{\frac{s}{\kappa_T}} r$.

It should be pointed out that the integral constant could be independently determined with temperature boundary conditions, say Equations (15) and (19).

Next, we shall take a look at the second equation, which is relatively difficult to be solved, given that it is not the standard form of the modified Bessel equation. However, we could find a particular solution for it,

$$p^{\circ*} = a \Delta T^{\circ} + b \quad (\text{A.12})$$

where

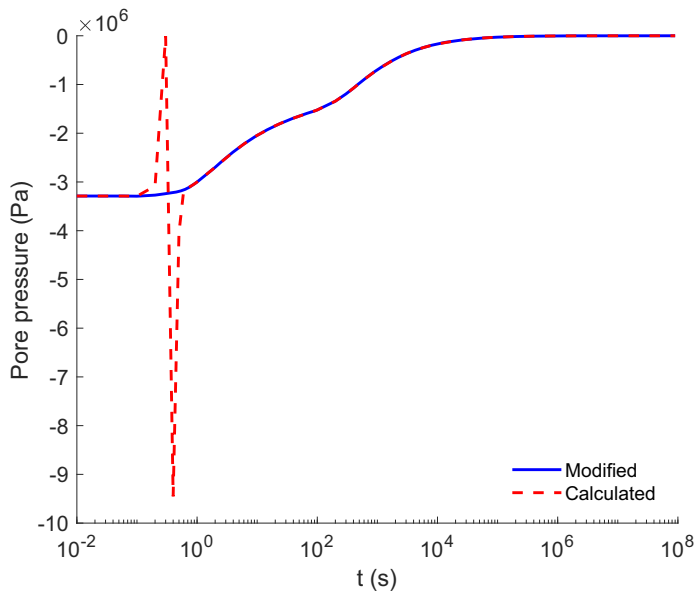


Figure B.1. Demonstration of modification made in Figure 3.

$$a = \frac{c_T}{1 - \frac{c}{\kappa_T}} \quad (\text{A.13})$$

$$b = -c_g g^\circ \quad (\text{A.14})$$

Therefore, the solution for pressure in Laplace domain is

$$p^0 = p^{\circ*} + C_3 I_0(\xi_p) + C_4 K_0(\xi_p) \quad (\text{A.15})$$

where $\xi_p = \sqrt{\frac{s}{c}} r$

With similar method, in which we derive Navier-type equations as above, in the Laplace domain, the solution of them become

$$\begin{aligned} u_r^\circ &= C_5 r + C_6 \frac{1}{r} \\ &+ \frac{\eta}{G} \left[a \left(C_1 \frac{I_1(\xi_T)}{\xi_T} r - C_2 \frac{K_1(\xi_T)}{\xi_T} r \right) + \frac{b}{2} r + C_3 \frac{I_1(\xi_p)}{\xi_p} r - C_4 \frac{K_1(\xi_p)}{\xi_p} r \right] \\ &+ \left(C_1 \frac{I_1(\xi_T)}{\xi_T} r - C_2 \frac{K_1(\xi_T)}{\xi_T} r \right) \frac{\eta_d}{G} \end{aligned} \quad (\text{A.16})$$

and

$$g^\circ = 2C_5 \quad (\text{A.17})$$

Other solutions are then obtained from Equations (A.3) to (A.5).

$$\begin{aligned} v_{rr}^\circ &= C_5 + C_6 \frac{1}{r^2} + \frac{\eta}{G} \left[a \left(C_1 \left(I_0(\xi_T) - \frac{I_1(\xi_T)}{\xi_T} \right) + C_2 \left(K_0(\xi_T) + \frac{K_1(\xi_T)}{\xi_T} \right) \right) + \frac{b}{2} \right. \\ &\quad \left. + C_3 \left(I_0(\xi_p) - \frac{I_1(\xi_p)}{\xi_p} \right) + C_4 \left(K_0(\xi_p) + \frac{K_1(\xi_p)}{\xi_p} \right) \right] \end{aligned} \quad (\text{A.18})$$

$$\begin{aligned} v_{\theta\theta}^\circ &= C_5 + C_6 \frac{1}{r^2} + \frac{\eta}{G} \left[a \left(C_1 \frac{I_1(\xi_T)}{\xi_T} - C_2 \frac{K_1(\xi_T)}{\xi_T} \right) + \frac{b}{2} + C_3 \frac{I_1(\xi_p)}{\xi_p} - C_4 \frac{K_1(\xi_p)}{\xi_p} \right] \\ &+ \frac{\eta_d}{G} \left(C_1 \frac{I_1(\xi_T)}{\xi_T} - C_2 \frac{K_1(\xi_T)}{\xi_T} \right) \end{aligned} \quad (\text{A.19})$$

$$q_r^\circ = -\kappa \left(a \sqrt{\frac{s}{\kappa_T}} (C_1 I_1(\xi_T) - C_2 K_1(\xi_T)) + \sqrt{\frac{s}{c}} (C_3 I_1(\xi_p) - C_4 K_1(\xi_p)) \right) \quad (\text{A.20})$$

Appendix B. Elaboration on modification of Figure 3

In this section, deficiencies of Stehfest algorithm are elaborated on its instability when the function to be inversed is rather complicated, as is the case in our model.

Basically, there are two points to point out:

First, in applying the algorithm devised by Stehfest (1970) to our model, the smaller the time where the inversion is carried out, the larger the value of Bessel function would be in calculation. Sometimes, its value would even overflow the range of double precision variables. In our work, such deficiency is overcome by applying multi-precision calculation, making it possible to calculate the time as small as 10^{-2} s, as in Figure 3.

Second, while with our effort, the curve could be rather smooth when calculating the pressure development in place relatively farther away from the diffusion boundary, say, the cement-formation interface, large inprecision is found for place closer, as in Figure 3 when radius equals to 0.155m. Such inprecision is demonstrated in Figure B.1 and may be attributed to the instability of Stehfest algorithm in calculating relatively complex functions.